Evidence for deep mantle upwellings beneath the equatorial Mid-Atlantic Ridge

Matthew R. Agius[1,2]*, Catherine A. Rychert[1], Nicholas Harmon[1], Saikiran Tharimena[1,3], J.-Michael Kendall[4]

[1]University of Southampton, United Kingdom. [2]Now at Università Roma Tre, Italy. [3]Now at Institute for Meteorology and Geophysics, University of Vienna, Austria. [4] University of Oxford, United Kingdom. *e-mail: matthew.agius@soton.ac.uk.

Summary

The location and degree of material transfer between the upper and lower mantle are key to Earth's thermal and chemical evolution. Sinking slabs and rising plumes are generally accepted as locations of transfer[1,2], whereas mid-ocean ridges are not typically assumed to play a role[3]. However, tight constraints from in-situ measurements at ridges have proven challenging. We use *P*-to-*S* receiver functions to image the mantle transition zone (MTZ) discontinuities using ocean bottom seismic data from the equatorial Mid-Atlantic Ridge (MAR). We image the 660 km discontinuity broadly uplifted by 10 ± 4 km over a ~600 km swath with the 410 km discontinuity depressed by 5 ± 4 km. The thin MTZ is coincident with slow mantle shear wave velocities from global seismic tomography[4,5,6,7]. In addition, MTZ velocities beneath the MAR are on average slower than those beneath older Atlantic seafloor. The observations imply material transfer between the upper and lower mantle, either continuous or punctuated, that is linked to the MAR. Given the length and longevity of the mid-ocean ridge system, it implies whole mantle convection may be more prevalent than previously thought, with ridge upwellings playing a role in counter balancing slab downwellings.

The mantle transition zone, the region located between 410 and 660 km depth[8], acts as the gatekeeper between the upper and lower mantle. It is bounded by phase changes and associated density variations that are thought to impact material transfer, thus controlling convection between the upper and lower mantle. A host of observations from geophysics and geochemistry have been used to constrain material transfer across the transition zone, particularly at hotspots and subduction zones. Seismic tomography images velocity anomalies interpreted as ascending plumes[7,9,10] and descending slabs[11,12] that cross the transition zone. Seismic images of deflections of the velocity discontinuities that bound the transition zone are consistent with mineral physics predictions[13] for upwellings beneath ocean islands and downwellings near subduction zones[14,15]. Ocean island trace element and isotopic signatures are typically thought to originate from the lower mantle, although their uniqueness in comparison to other global rock compositions is often interpreted in support of a geochemically distinct lower mantle that has not been well-mixed with the upper mantle. Similarly, discrepancies among composition of the chondritic Earth, noble gasses in the atmosphere, the continental crust and mid-ocean ridge basalts are often thought to indicate a distinct lower mantle reservoir, less obviously consistent with whole mantle mixing[3].

Several models have been proposed to explain the observations from geophysics and geochemistry. Distinct geochemical signatures could originate from pockets of enrichment in a generally heterogeneous Earth[16], isolated chemical piles[17,18,19,10] that cause sluggish convection at >1000 km depth[10], compositional layering[20] caused by slab stagnation at 660 or 1000 km[21,22], or stable lower mantle convective domains of intrinsically strong $(Mg,Fe)SiO_3$-bridgmanite in low-Mg/Si domains[23]. Alternatively, the mantle may pervasively rise across the transition zone, but typically be compositionally filtered during the process[24]. High-resolution seismic imaging is required to better constrain these dynamics, which has remained challenging given that 70% of the Earth surface is under water.

The mid-ocean ridge system comprises Earth's longest tectonic boundary and is a region of associated upwelling responsible for the generation of massive quantities of oceanic crust that covers most of the Earth, although it is generally considered insignificant in whole-scale mantle convection. Mid-ocean ridge basalt geochemistry is characterized by depletion of incompatible elements, much different than the enriched ocean island basalts from hot-spots related to plumes. Therefore, mid-ocean ridges are typically interpreted as melting of a relatively depleted uppermost mantle[3], without a connection to the lower mantle. Similarly, neither seismic tomography nor the deflection of the bounding seismic velocity discontinuities of the transition zone have been interpreted in terms of material transfer beneath ridges. The lateral resolution of seismic tomography at transition zone depths beneath ridges is typically broad, ≥ 500 km in global tomography models, and only a bit smaller, 300–400 km, in regional scale full-waveform models[9]. Similarly, given the remoteness of ridges, most imaging of sub-ridge MTZ discontinuities comes from *SS* precursor studies, which sample locations where station coverage is sparse but also have broad ~10° lateral resolution[14,15]. *P*-to-*S* (*Ps*) receiver functions provide some of the highest resolution imaging of MTZ discontinuities, although these studies are generally limited to terrestrial regions, including ocean islands above plumes, where most seismic stations are located.

We imaged the MTZ discontinuities beneath the equatorial Mid-Atlantic Ridge (MAR) using *Ps* receiver functions. We used data from ocean bottom seismometers (OBS) deployed as part of the Experiment to Unearth the Rheological Oceanic Lithosphere-Asthenosphere Boundary (EURO-LAB) and the Passive Imaging of the Lithosphere-Asthenosphere Boundary (PI-LAB) experiment at the equatorial Mid-Atlantic Ridge from March 2016 – March 2017 (Fig. 1). We performed an extended time multi-taper deconvolution to determine the *P*410*s* and *P*660*s* conversions and migrated the waveforms to depth along the theoretical ray paths into a 3-D grid using a crust-corrected 3-D velocity model[7] (see Methods for details and testing).

We image positive peaks (velocity increases with depth) associated with the 410- and 660-km discontinuities across a broad ~1000-km wide area, centred at the ridge to about 80 Myr old lithosphere (Figs. 2 and 3). In the eastern part of our study area the MTZ thickness is 240–250 km consistent with predictions for typical mantle conditions[14,15] and the observed global average from *P*-to-*S* receiver functions of 246.1 km[25]. In the west the 410 is depressed by 5 ± 4 km over a 300 km swath of mantle and the 660 is uplifted by 10 ± 4 km over a 600 km swath, centred beneath the Romanche Fracture Zone between two adjoining ridge segments, with slightly stronger anomalies in more localized regions, 10 ± 4 km for the 410 and 15 ± 4 km for the 660. The topography changes of the 410 and 660 discontinuities are vertically aligned, with the 660 having a large and broad depth change, resulting in the MTZ thinning of up to 15 ± 8 km over ~600 km, associated with stronger thinning (20 km) in a smaller area (~200 km) (Figs. 2 and 3). Testing indicates that our observations are robust, and the imaged depth variabilities of the interfaces are unlikely to be an artefact of velocity anomalies in the upper mantle atop of the MTZ or within it (Methods).

We also image negative phases just shallower than both the 410 and 660 km discontinuities at 353–367 and 598–607 km, in at least some portions of our study region (Fig. 4) with an increase in the amplitude of the supra-410 in the west. However, more testing is required to establish robustness and the structures required by the data (Methods), which is beyond the scope of this paper. Therefore, we do not interpret them in any detail.

Although MTZ thinning beneath a mid-ocean ridge has yet to be proposed, when the resolution of previous studies is considered, our result is not inconsistent with previous global and regional imaging or sparse previous reports at a local-to-regional scale. The limited lateral scale of the region with the strongest observed thinning (~200 km) could explain why several *SS* precursor models with broad ~10° sensitivity have not previously detected mid-ocean ridge related thinning[14,15]. Similarly, a single stack of *P*-to-*S* receiver functions averaged over the entire region from the Mantle Electromagnetic and Tomography (MELT) Experiment at 17°S on the East Pacific Rise did not detect thinning. However, testing from this study indicated limited resolution precluded imaging a feature characterized by $<$10-15 km thinning over a region $<$ 300 km wide, and/or centred $>$ 300 km off-axis[26]. In other words, the size, scale, and location of our observation is at the very edge of the resolution of the previous study. A thinned transition zone was also reported by a single stack of *Ps* receiver functions using a short term, small aperture ocean bottom array at the ultra-slow spreading Southwest Indian Ridge, although with a slightly larger magnitude (26–30 km vs. 15 ± 8 km), and also general resolution uncertainty given that it is a point measurement[27]. Our result is also consistent with a hotspot-focused *SS*- and *PP*-precursor study located tens of degrees northeast of our study area; besides hotspot-related thinning, the study imaged the 660 uplifted by 15 ± 7 to 26 ± 5 km vs. 10 ± 4 km in bounces closer to the mid-Atlantic Ridge[28]. These observations of mid-ocean ridge related transition zone thinning suggest it could be a common feature of ridges or at least for slow or ultra-slow spreading ridges.

Our study area is likely representative of relatively normal mid-ocean ridge with little to no influence from hotspots. The nearest hotspot to our study area is located > 700 km to the south at Ascension Island (Fig. 4), and Ascension is not classified as a primary plume with deep mantle origin[29]. The location of our thinned MTZ anomaly is not linked to Ascension via tomographic anomaly, but rather associated with a slow seismic velocity anomaly that extends vertically through the mantle to our study area in global tomography models, e.g., PRI-S05[7].

Upwelling from the lower mantle beneath broader sections of the mid-Atlantic Ridge is also generally supported by global seismic tomography models and geochemistry. MTZ velocities are on average slower beneath the MAR than beneath older, more distant Atlantic lithosphere (Methods, Extended Data Figs. 1 and 2). The slow sub-ridge MTZ velocity anomalies occur with a more punctuated character in some models. Therefore, the ridge anomalies could be more or less continuous in space and/or time given trade-offs in resolution of the tomography models at these depths. Several locations along the MAR axis are also characterized by mildly enriched isotopic signatures[30], at least relative to the typical depleted ridge character, without necessarily being directly linked to a plume, lending additional support for a lower mantle origin beneath the MAR. Overall, this suggests that ridge-related upwelling may be common along the Atlantic. Furthermore, our tests suggest that slow seismic velocities in the transition zone could exist beneath other ridges in some global seismic models, suggesting ridge-related transition zone thinning and upwelling could be even more widespread, potentially with different scales or frequency of the punctuated anomalies (Extended Data Fig 2, Methods). Alternatively, the MAR may be different than fast spreading ridges like the EPR. In the lower mantle beneath the transition zone there is a lower degree of agreement among models.

Upwellings from the lower mantle are typically associated with strong thermal anomalies that result in volcanic ocean islands, with isotopically enriched magmatic signatures; whereas, mid-ocean ridge basalts are not typically characterized by subaerial topography, strong thermal anomalies or compositions that are as enriched as ocean islands. So, ridge upwellings must be different from plumes.

First, mid-ocean ridge upwellings from the lower mantle could be cooler and more sluggish than hotspots. Indeed, the thermal contrast implied by the observed thinning is generally less than that reported at hotspots. The 15 km of observed thinning corresponds to a predicted thermal anomaly of 115 K (see Methods for details, Extended Data Fig. 3), which is more muted than the 250–555 K anomaly inferred beneath Iceland[31]. The more muted (5 ± 4 km) 410 depression in comparison to 660 might also imply that material transfer across the MTZ is relatively sluggish, allowing for temperature reduction via conductive cooling. The inferred anomaly at the 410 (60 K) is also less than that inferred based on the 410 beneath Hawaii (119 K)[32]. If ridge-related upwellings are sluggish relative to plumes it could also reduce the isotopic signatures that reach the surface. For instance, these signatures could partition into a dense melt layer just above the 410 and/or the 660 discontinuities[24,33], and the negative supra-410 we observe could be consistent with such a model (Fig. 4; also see Methods).

Second, the lower mantle source material could be different and less isotopically enriched than that of ocean islands. For instance, it could originate from the relatively weak and depleted material surrounding the proposed strong, sluggish bridgmanite lower mantle convective domains that preferentially supply hotspots and aid geographic stability though time[23]. Or, the source could be a mixture of the two.

Finally, additional cooling and/or mixing of isotopic signatures could occur when the sluggish upwelling is entrained in more vigorous flow in the upper mantle[10,34]. Further cooling of the material that reaches the surface could also occur via small-scale convection[35] over a broad area. Sporadic isotopic enrichment along the MAR is similarly hypothesized to be the result of complex mixing in the upper mantle[**Error! Bookmark not defined.**,36], lending support for our model.

Our observations suggest greater links between whole mantle convection and surface tectonics at least beneath slow-spreading ridges. Given this and the longevity of the mid-ocean ridge systems over billion-year time scales, a greater degree of whole mantle convection occurs than in that of the classical models. The observed mid-ocean ridge upwellings likely play a role in counter balancing slab downwellings and should be accounted for in models of the thermal evolution of the Earth. Lower mantle upwellings beneath ridges may help to drive spreading, and this could be important in the absence of surrounding slab subduction forces. More work is required to establish this.

References from main text

1. Van der Hilst, R. D. Complex morphology of subducted lithosphere in the mantle beneath the Tonga trench. *Nature* **374**, 154-157 (1995).

2. Montelli, R., Nolet, G., Dahlen, F. A., Masters, G., Engdahl, E. R., & Hung, S. H. Finite-frequency tomography reveals a variety of plumes in the mantle. *Science* **303**, 338-343 (2004).

3. Hofmann, A. W. Mantle geochemistry: the message from oceanic volcanism. *Nature* **385**, 219 (1997).

4. Chang, S. J., Ferreira, A. M., Ritsema, J., van Heijst, H. J., & Woodhouse, J. H. Joint inversion for global isotropic and radially anisotropic mantle structure including crustal thickness perturbations. *J. Geophys. Res*. **120**(6), 4278-4300 (2015).

5. Ritsema, J., Deuss, A. A., Van Heijst, H. J., & Woodhouse, J. H. S40RTS: a degree-40 shear-velocity model for the mantle from new Rayleigh wave dispersion, teleseismic traveltime and normal-mode splitting function measurements. *Geophys. J. Int.* **184**, 1223-1236 (2011).

6. French, S., Lekic, V., & Romanowicz, B. Waveform tomography reveals channeled flow at the base of the oceanic asthenosphere. *Science* **342**, 227-230 (2013).

7. Montelli, R., Nolet, G., Dahlen, F. A., & Masters, G. A catalogue of deep mantle plumes: New results from finite-frequency tomography. *Geochem. Geophys. Geosyst.* **7**(11) (2006).

8. Dziewonski, A. M., & Anderson, D. L. Preliminary reference Earth model. *Phys. Earth Planet Inter.* **25**, 297-356 (1981).

9. Rickers, F., Fichtner, A., & Trampert, J. The Iceland–Jan Mayen plume system and its impact on mantle dynamics in the North Atlantic region: evidence from full-waveform inversion. *Earth Planet. Sci. Lett.* **367**, 39-51 (2013).

10. French, S. W., & Romanowicz, B. Broad plumes rooted at the base of the Earth's mantle beneath major hotspots. *Nature* **525**, 95-99 (2015).

11. Fukao, Y., & Obayashi, M. Subducted slabs stagnant above, penetrating through, and trapped below the 660 km discontinuity. *J. Geophys. Res.* **118**, 5920-5938 (2013).

12. Li, C., van der Hilst, R. D., Engdahl, E. R., & Burdick, S. A new global model for P wave speed variations in Earth's mantle. *Geochem. Geophys. Geosyst.* **9**(5) (2008).

13. Ito, E., & Katsura, T. A temperature profile of the mantle transition zone. *Geophys. Res. Lett.* **16**, 425-428 (1989).

14. Lawrence, J. F., & Shearer, P. M. Imaging mantle transition zone thickness with SdS-SS finite-frequency sensitivity kernels. *Geophys. J. Int.* **174**, 143-158 (2008).

15. Houser, C., Masters, G., Flanagan, M., & Shearer, P. Determination and analysis of long-wavelength transition zone structure using SS precursors. *Geophys. J. Int.* **174**, 178-194 (2008).

16. Morgan, J. P., & Morgan, W. J. Two-stage melting and the geochemical evolution of the mantle: a recipe for mantle plum-pudding. *Earth Planet. Sci. Lett.*, **170**(3), 215-239 (1999).

17. Jellinek, A. M., & Manga, M. The influence of a chemical boundary layer on the fixity, spacing and lifetime of mantle plumes. *Nature* **418**, 760-763 (2002).

18. Jellinek, A. M., & Manga, M. Links between long-lived hot spots, mantle plumes, d″, and plate tectonics. *Rev. Geophys.* **42**(3) (2004).

19. McNamara, A. K., & Zhong, S. Thermochemical structures beneath Africa and the Pacific Ocean. *Nature* **437**, 1136-1139 (2005).

20. Kellogg, L. H., Hager, B. H., & van der Hilst, R. D. Compositional stratification in the deep mantle. *Science* **283**, 1881-1884 (1999).

21. Ballmer, M. D., Schmerr, N. C., Nakagawa, T., & Ritsema, J. Compositional mantle layering revealed by slab stagnation at~ 1000-km depth. *Sci. Adv.* **1**(11) (2015).

22. Marquardt, H., & Miyagi, L. Slab stagnation in the shallow lower mantle linked to an increase in mantle viscosity. *Nat. Geosci.* **8**, 311-314 (2015).

23. Ballmer, M. D., Houser, C., Hernlund, J. W., Wentzcovitch, R. M., & Hirose, K. Persistence of strong silica-enriched domains in the Earth's lower mantle. *Nat. Geosci.* **10**, 236-240 (2017).

24. Bercovici, D., & Karato, S. I. Whole-mantle convection and the transition-zone water filter. *Nature* **425** (2003).

25. Lawrence, J. F., & Shearer, P. M. A global study of transition zone thickness using receiver functions. *J. Geophys. Res.* **111** (2006).

26. Shen, Y., Sheehan, A. F., Dueker, K. G., de Groot–Hedlin, C., & Gilbert, H. Mantle discontinuity structure beneath the southern East Pacific Rise from P-to-S converted phases. *Science* **280**, 1232-1235 (1998).

27. Ruan, A., Hu, H., Li, J., Niu, X., Wei, X., Zhang, J., & Wang, A. Crustal structure and mantle transition zone thickness beneath a hydrothermal vent at the ultra-slow spreading Southwest Indian Ridge (49° 39′ E): a supplementary study based on passive seismic receiver functions. *Mar. Geophys. Res.* **38**, 39-46 (2017).

28. Saki, M., Thomas, C., Nippress, S. E., & Lessing, S. Topography of upper mantle seismic discontinuities beneath the North Atlantic: The Azores, Canary and Cape Verde plumes. *Earth Planet. Sci. Lett.* **409**, 193-202 (2015).

29. Courtillot, V., Davaille, A., Besse, J., & Stock, J. Three distinct types of hotspots in the Earth's mantle. *Earth Planet. Sci. Lett.* **205**, 295-308 (2003).

30. Jenkins, J., Cottaar, S., White, R. S., & Deuss, A. Depressed mantle discontinuities beneath Iceland: Evidence of a garnet controlled 660 km discontinuity? *Earth Planet. Sci. Lett.* **433**, 159-168 (2016).

31. Agius, M. R., Rychert, C. A., Harmon, N., & Laske, G. Mapping the mantle transition zone beneath Hawaii from Ps receiver functions: Evidence for a hot plume and cold mantle downwellings. *Earth Planet. Sci. Lett.* **474**, 226-236 (2017).
32. Dalton, C. A., Langmuir, C. H., & Gale, A. Geophysical and geochemical evidence for deep temperature variations beneath mid-ocean ridges. *Science* **344**, 80-83 (2014).
33. Richter, F. M. Convection and the large-scale circulation of the mantle. *J. Geophys. Res.*, **78**, 8735-8745 (1973).
34. Le Voyer, M., Cottrell, E., Kelley, K. A., Brounce, M., & Hauri, E. H. The effect of primary versus secondary processes on the volatile content of MORB glasses: An example from the equatorial Mid-Atlantic Ridge (5°N–3°S). *J. Geophys. Res.* **120**, 125-144 (2015).
35. Schilling, J. G., Hanan, B. B., McCully, B., Kingsley, R. H., & Fontignie, D. Influence of the Sierra Leone mantle plume on the equatorial Mid-Atlantic Ridge: A Nd-Sr-Pb isotopic study. *J. Geophys. Res.* **99**, 12005-12028 (1994).
36. Thomson, A. R., Walter, M. J., Kohn, S. C., & Brooker, R. A. Slab melting as a barrier to deep carbon subduction. *Nature* **529**, 76 (2016).
37. Bird, P. An updated digital model of plate boundaries. *Geochem. Geophys. Geosyst.* **4** (2003).

Acknowledgements C.A.R. and N.H. acknowledge funding from the Natural Environment Research Council (NE/M003507/1 and NE/K010654/1) and the European Research Council (GA 638665). J.M.K. was funded by the Natural Environment Research Council the Natural Environment Research Council (NE/M004643/1). We thank the captain and crew of the R/V Marcus G. Langseth and the RRS Discovery and also the scientific technicians. We thank two anonymous reviewers for helpful comments and suggestions.

Author contributions M.R.A. processed the data and wrote the manuscript. C.A.R. conceived the experiment, acquired funding, managed the project, and wrote the manuscript. N.H. contributed to conceptualization, funding acquisition, project management, and writing of the original manuscript. S.T. organized the raw data and assisted in initial data quality control. J.M.K. contributed to funding acquisition and the writing of the manuscript.

Competing interests The authors declare no competing interests.

Data availability Data are available from the Incorporated Research Institutions for Seismology (IRIS) DMC website https://ds.iris.edu/ds/nodes/dmc/ under the XS network for 2016-2017 (https://doi.org/10.7914/SN/XS_2016).

Code availability The methods and codes used are standard and widely used (Helffrich, 2006)[42] and are detailed in the Methods section. Figures were made using Generic Mapping Tools[xx] and MATLAB[yy]. Correspondence and requests for materials should be addressed to M.R.A. (matthew.agius@soton.ac.uk).

Main figure legends

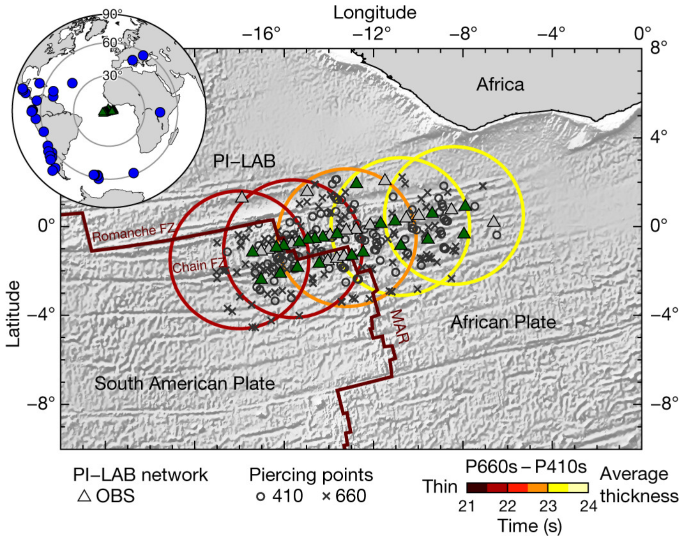

Fig. 1 | The PI-LAB network, data coverage and mantle transition zone delay time. 39 OBS stations (triangles) cover a broad area across the equatorial Mid-Atlantic Ocean. 48 teleseismic earthquakes (insect map, blue dots) located between 35°–80° epicentral distance (grey concentric circles on global map) away from the network produced 241 high-quality waveforms recorded at stations indicted by green triangles. Open circles and crosses indicate piercing points at 410- and 660-km depth, respectively. Large coloured circles indicate delay time differences between *P*660*s* and *P*410*s* in waveforms stacked in 3°-radius bins. Red line marks the Mid-Atlantic Ridge[37].

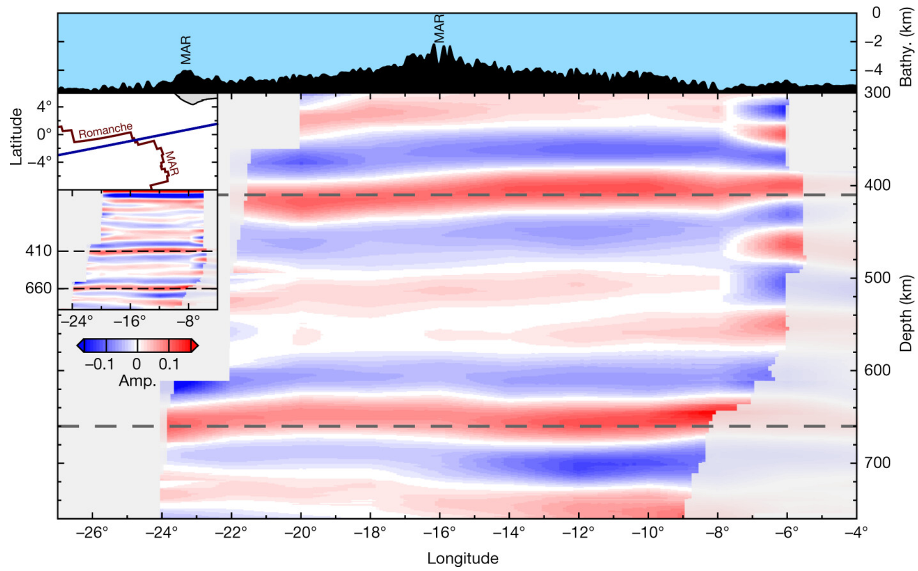

Fig. 2 | Vertical cross-section from the 3-D depth migrated receiver functions. Red and blue shades represent positive and negative amplitudes saturated at ±0.17, respectively. Inset map: Location of the cross-section (blue line). Red line marks the Mid-Atlantic Ridge (MAR)[37]. Inset cross-section: The entire depth cross section from the surface down to 800-km depth. Semi-transparent shades: Poorly constrained areas. Dashed lines: 410- and 660-km depths. Depths are with respect to sea level. Top: Average bathymetry across the transect.

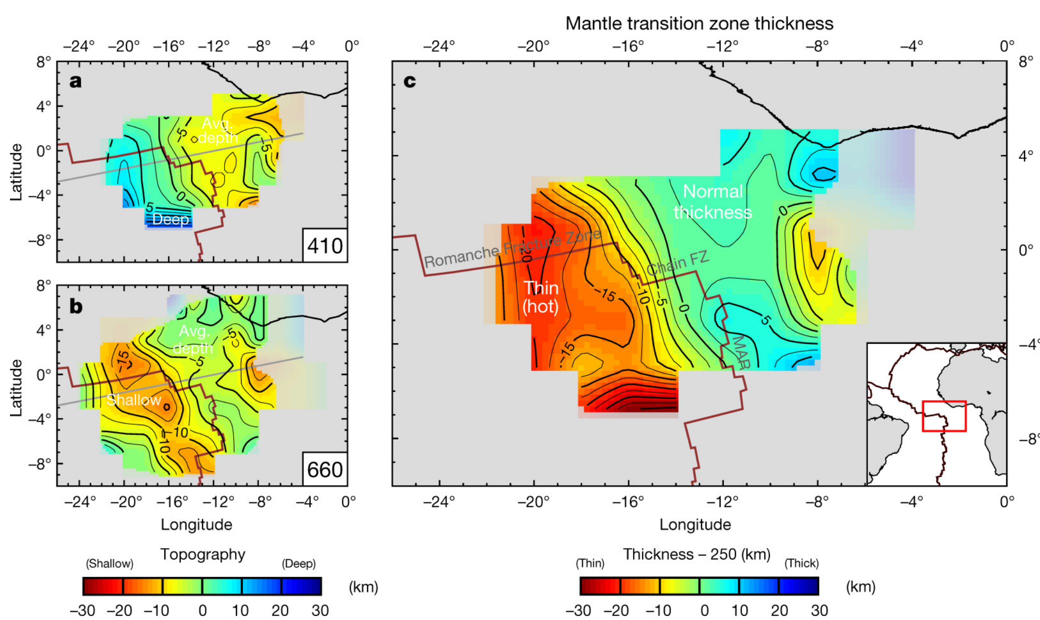

Fig. 3 | Horizontal cross-sections from the 3-D depth migrated receiver functions. a, Red and blue shading represent a shallower and deeper 410-km discontinuity, respectively. **b**, Same as **a**, but for the 660-km discontinuity. **c**, Red and blue shading indicates a thinner and thicker mantle transition zone, respectively. Semi-transparent shades are poorly constrained areas. Grey line shows the location of the vertical cross section in Fig. 2. Inset map shows the study area on a regional map. Red line marks the Mid-Atlantic Ridge[37].

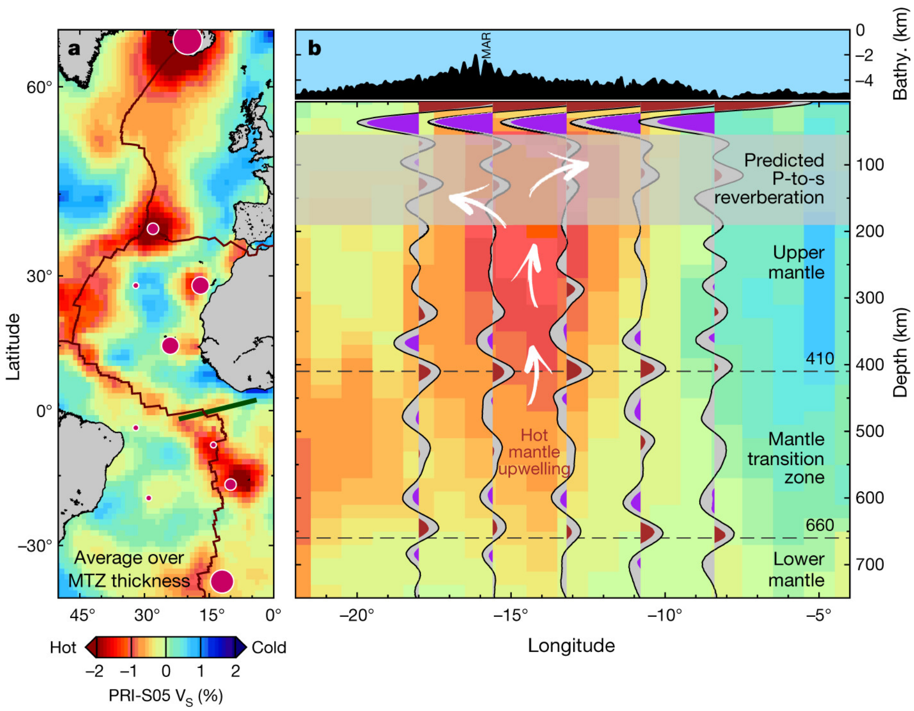

Fig. 4 | Mantle flow beneath the Mid-Atlantic Ridge. a, Map of average shear-velocity anomalies within the mantle transition zone from global seismic tomography PRI-S05[7]. Pink circles show regional hotspots scaled according to their deep origin ranking[29] (Methods). Green line: Location of the cross section (right). Red line: Plate boundaries[37]. **b**, Vertical cross section showing the shear velocity anomalies overlaid by depth migrated receiver functions (black wiggles) from binned areas (Fig. 1). Brown (positive)/purple (negative) shaded part of wiggles are 95% confidence level of the receiver function from bootstrap resampling. Background colour indicates seismic velocities from PRI-S05[7]. White arrows indicate inferred mantle flow.

Methods

Seismic data. The data is from ocean bottom seismometers deployed during the PI-LAB and EURO-LAB experiments from 2016–2017. The stations were a combination of broadband 120-s and 240-s period instruments spread out across both sides of the mid-Atlantic ridge and centred on the Chain Fracture Zone[38,39] (Fig. 1). Pre-processing of the waveforms included the removal of tilt noise on the vertical components[40], the removal of compliance noise[41], reorientation of the horizontal components into the radial and transverse components using estimated orientation from *P*-wave polarization[38], demeaning the data, and applying a zero-phase, fourth order Butterworth filter from 0.05–0.2 Hz. Although we used tilt and compliance corrected data in the final model, we also explored the effect of this assumption. We compared corrected and uncorrected raw data both unfiltered and in the frequency band used in this experiment. While the corrections are visible in the unfiltered data, once filtered, the corrected and uncorrected data are indistinguishable in the majority of cases. We present some example waveforms in Extended Data Fig. 4.

Receiver functions. We determined *Ps* receiver functions to illuminate the MTZ discontinuities and thickness beneath the equatorial MAR. Each earthquake waveform was manually inspected. Records with a clear *P*-wave phase within 5 seconds of the theoretical arrival were selected. This signal was then deconvolved from the radial component using the extended multitaper frequency domain deconvolution technique[42] to produce a receiver function. A positive amplitude receiver function phase indicates a velocity increase with depth, whereas a negative amplitude indicates a velocity decrease. Naturally, data from OBS stations tend to have a higher noise level and thus required careful selection. We inspected each receiver function, discarded waveforms with unstable deconvolutions (pure ringing), and only selected cases with a clear *Ps* phase amplitude of 0.2 for the Mohorovičić discontinuity and 0.1 for 410 and 660 discontinuities (*P*410*s* and *P*660*s*, respectively) using theoretical arrival times as a guide. Where necessary, the *P* wave was re-examined and the receiver function reviewed. Most receiver functions have all three phases present, but in an effort to maximize the potential use of as many waveforms as possible, in cases where one phase was clear and the other was obscured by ringing, individual datasets were selected for the *P*410*s* and the *P*660*s*. These waveforms had to have a good Moho phase and a good signal for the respective phase. The laterally coherent arrivals from the receiver function show strong illumination at the 410- and 660-km depth discontinuities (Fig 2).

In total, 22 ocean-bottom seismometers provided 241 waveforms of 48 teleseismic earthquakes with a magnitude greater than 5.5 and with an epicentral distance to the stations between 35° and 80°. The *P*410*s* data set comprised of 160 waveforms whereas the *P*660*s* data set comprised of 146 waveforms. The piercing points from the respective data sets are shown in Fig. 1 and the corresponding hit map in Extended Data Fig. 5.

The delay time difference between the *P*660*s* and the *P*410*s* phases east of our study area is 23.5 seconds, indicative of average MTZ thickness. The delay decreases towards the west, down to 21.5 s suggesting a thinner MTZ (Fig. 1).

We find that receiver functions calculated using the tilt and compliance corrected and uncorrected data are nearly identical to those calculated from uncorrected data (Extended Data Fig. 4).

Depth migration. Each receiver function is migrated to depth using the global Earth compressional- and shear-velocity model PRI-P05 and PRI-S05[7]. Corrections for the negative station elevation were applied such that discontinuity depths are with respect to sea level. The migrated receiver function were then back projected along the theoretical ray path and stacked onto a three-dimensional grid[43,32] that has a lateral spacing of 2º by 2º and a 1-km depth vertical spacing. The grid is then smoothed with a radius corresponding to the Fresnel zone of the waveform determined by $\sqrt{\left(\frac{\lambda}{2}+d\right)^2-d^2}$, where λ is the wavelength and d is the depth. Extended Data Fig. 5 shows the hit map and spread at 410 and 660 km depths. Because of the separate selection of the *P*410*s* and *P*660*s* phases, we generate two 3-D grids, which are then merged into a single grid using a linear weighting between 410- to 660-km depth of the grids.

Receiver function uncertainties. We estimated receiver function uncertainties with bootstrap resampling to assess the signal coherence and stability from 100 randomly selected traces within a sample[44] (Fig. 4). Figure 4 shows the averaged receiver function traces with clear positive (brown) peak at about 410 and 660-km depth, as well as at '520-km' depth. The amplitude of the uncertainty (2σ) is shown in grey bands. The standard errors of the depth of the 410 and 660 km discontinuities were determined based on the depth range of the peak of the stacked waveforms (Extended Data Fig. 6).

We performed preliminary testing of the negative supra-410 and supra-660 phases observed in the data, in particular for receiver functions that appeared asymmetric, with smaller negative sidelobe following the main 410 and 660 phases. We compared the waveforms to synthetics with a simple PREM model both including and excluding the water layer, and applying processing and filtering applied to the data. We found that several of the amplitudes of several supra-410 phases in particular required a supra-410 low velocity layer to achieve large enough amplitudes to match those of the supra-410 phases. However, to fully explore the structures required by the data, it would require testing that is beyond the scope of the current work.

A phase in the upper mantle at 200 - 300 km depth in one waveform stack (Fig. 4) is visible, but not persistent across the array. It is likely related to previously reported sporadic phases at these depths globally that could possibly be caused by small scale heterogeneity[45].

Migration tests on transition zone thickness. We perform a number of tests to show that the observed phases and their depth variability are robust regardless of assumptions such as migration model. To minimize the effects of the shallow migration model we difference the discontinuity depths and consider transition zone thickness. Clear thinning is observed (Fig. 3). We also test the effect of a variety of migration models for the entire upper mantle down to the base of the transition zone. Given the sensitivity of the depth migration to Vp/Vs ratio, the PRI[7] model, used in the main text Figures, was a natural choice, in comparison to other shear wave velocity models. However, we also tested a global surface wave velocity model of V_S (SEMUM2)[6] and assuming V_P/V_S from PREM[8], and also a simple 1-D global model (V_P and V_S) appropriate for the oceans (Extended Data Fig. 7). This range of models encompasses the state of the art velocity models available, accounting for 3D variability. The difference in our result assuming the 3D vs. the 1D models provides a good estimate for the maximum effect of velocity model on our results. Regardless of the migration model assumptions, all give the same pattern and all show a depressed 410, and elevated 660 and a thinned transition zone. Differences for the 410, 660, and MTZ thickness range of 5, 7.5 and 7.5 km, respectively. SEMUM2 yields the largest anomalies at 660 and MTZ thickness. Irrespective of which background model is used, the MTZ discontinuities have coherent stacking.

We also tested the effect of using receiver functions calculated using data without the tilt and compliance corrections. The amount of transition zone thinning in the fully migrated model is also very similar regardless of the correction, with only a slightly larger phase amplitudes and MTZ thinning. However, nowhere in the model did the thinning exceed the error of our result and the maximum difference was < 2 km. In the end, the data correction may help in terms of picking data, but we do not find a significant difference in the final result using corrected or uncorrected data.

Temperature estimates. Temperature anomalies from the mantle adiabat in the depth range of the MTZ have an effect on the 410 and 660 phase transformations, which are controlled by pressure-temperature Clapeyron slopes[46,47]. Thus, changes in the depth of the discontinuities serve as a thermometer. For example, a hotter MTZ as a result of upwelling will yield the 410-km discontinuity to deepen (higher pressure) and the 660-km discontinuity to rise (lower pressure), consequently thinning the transition zone, whereas a cooler MTZ as a result of a subducting slab yields a thicker transition zone. Furthermore, the presence of anomalous water may displace the phase transition boundaries such that the 410-km discontinuity becomes shallower and the 660-km discontinuity deeper[48].

We determine 3 temperature estimates for the MTZ using relationships of temperature with thickness and with discontinuity depths. We assume that perturbations to the discontinuity depths are due to temperature-induced changes alone neglecting any effects of composition. Two temperature estimates are obtained from the discontinuity depth changes using experimental relationships based on pressure and mineral phase transitions: +2.9 MPa/K at the 410-km depth discontinuity[46], and -2.5 MPa/K at the 660-km depth discontinuity[47] (Extended Data Fig. 3). Depth changes in the range of +5 to 8 and -10 to -15 km depth, respectively, imply an excess temperature of +60–97 K and +140–210 K, respectively (Fig. 3 and Extended Data Fig. 3). We prefer the more conservative (smaller) values and present those in the main text. The temperature estimate based on MTZ thickness is inferred from a joint study of *Ps* receiver functions with shear velocity -0.13 ± 0.07 km/K[49] using similar derivatives. A conservative 15 ± 8 km decrease in thickness results in an average temperature excess of 115 ± 62 K (Extended Data Fig. 3).

These temperature estimates depend on the values used for the Clapeyron slopes, which can range from 1.5–2.9 MPa/K and from -4.0 to -2.0 MPa/K for the phase transition at 410- and 660-km depth[47,50,51], respectively, as well as on the migration model used. For example, with SEMUM2[6] the thermal anomalies at the 410, 660 and from the MTZ thickness result in higher values reaching 186, 246 and 208 K, respectively. Water too may have a role, which if anomalously present, will result in a shallow 410 and a depressed 660 km discontinuity[52], however, this is not observed. Similarly, no deepened 660 km discontinuity is noticed that may have resulted from a post-garnet transition[31].

Hotspot plot and ranking. Regional hotspots were scaled to their deep origin ranking[29] and plotted accordingly[29,53].

Statistical evaluation of seismic velocities in the transition zone in global and regional models. We tested the hypothesis that the mean velocity in the mantle transition zone beneath the mid-Atlantic ridge is slower than the mean velocity beneath older, more distant Atlantic seafloor in a range of publicly available global and regional velocity models. We tested global models SGLOBE[4], S40RTS[5], PRI-05[7], SEISGLOB2[54], SEMUCB[55], SPani[56] and S362ANI+M[57]. We also tested the regional CSEM full waveform models of the North Atlantic[9] and South Atlantic[58]. We interpolated the models onto a common grid of evenly distributed nodes on the surface of the globe, approximately 2° apart. We binned by distance to the nearest ridge. We tested a range of bin sizes. We present 300 km half-width bins (600 km total, symmetric about the ridge-axis), which is on the order of the lateral resolution of most global tomography, ~5° or greater. The majority of our observed transition zone anomaly would also fall within a ridge bin of this dimension, given that the thinning is centred beneath the Romanche Fracture Zone, between two adjoining ridge segments. However, we also tested 400-600 km bin half widths which would completely encompass our observed anomaly. We averaged the velocities in the global models from 400 to 700 km depth, and we averaged the velocities in the regional Atlantic models from 410 to 500 km depth, the deepest depth that was publicly available. Continental nodes and nodes that were within 6 degrees of a known hotspots compilation[29,53] were excluded from the averages. We calculated the one-tailed t-statistic assuming unequal variance, which had ~350 degrees of freedom for global models and ~120 and ~250 degrees of freedom for North and South Atlantic regional models estimated using Satterthwaite's approximation. For this number of degrees of freedom, the absolute value the t-statistic must exceed ~1.67 and ~2.37 to reject the null hypothesis at 95 % and 99 % probability, respectively.

We find that for 8 out of 9 velocity models there is at least a >95% probability that the mean of the average velocity of the mantle transition zone within 300 km of the mid-Atlantic ridge is smaller than that beneath older, more distant seafloor. The only model for which the hypothesis failed was S362ANI+M, which had a small positive t-statistic suggesting that the mean velocity is faster beneath the mid-ocean ridge than more distant seafloor, even if it is not statistically significant. Histograms of the binning and averaging of the models are shown in Extended Data Figs. 1 and 2, with error bars corresponding to the standard error of the mean for each bin. We also show the mean of the non-ridge bins in red. Two models, SEISGLOB2 and CSEM N Atlantic have mean values that are offset from the maxima in the histograms, which is due to distributions that have broad positive tails that extend off the figure limits. For the larger half bin widths up to 600 km, again, all models except S362ANI+M had at least a >95% probability as might be expected given the trends visible in Extended Data Fig 1.

We performed a similar test on the entire global mid-ocean ridge system and found that average transition zone velocities within 300 km of the ridge were slower than those beneath more distant seafloor in 3 (PRI-S05, S40RTS and SEISGLOB2) out of the 7 global models at the 95% confidence limit. Larger bin sizes yielded the same result. This could be suggestive of a more global trend. However, the trend may, or likely does, occur at different scales for different spreading rates. Although more thorough testing may further illuminate these trends and the scales of the trends, further investigation is beyond the scope of our study. Alternatively, the phenomenon may be most prevalent at slower spreading centres and/or present along only some portions of the faster spreading mid-ocean ridge system. Given this uncertainty, we only recognise the possibility of global upwelling beneath mid-ocean ridges rather than emphasizing this point.

References only cited in the online Methods section

38. Agius, M. R., Harmon, N., Rychert, C. A., Tharimena, S., & Kendall, J. M. Sediment characterization at the equatorial Mid-Atlantic Ridge from P-to-S teleseismic phase conversions recorded on the PI-LAB experiment. *Geophys. Res. Lett.* **45**, 12-244 (2018).
39. Harmon, N., Rychert, C., Agius, M., Tharimena, S., Le Bas, T., Kendall, J. M., & Constable, S. Marine geophysical investigation of the chain fracture zone in the Equatorial Atlantic from the PI-LAB experiment. *J. Geophys. Res.* **123**, 11-016 (2018).
40. Crawford, W. C., & Webb, S. C. Identifying and removing tilt noise from low-frequency (< 0.1 Hz) seafloor vertical seismic data. *Bull. Seismol. Soc. Am.* **90**, 952-963 (2000).
41. Bell, S. W., Forsyth, D. W., & Ruan, Y. Removing noise from the vertical component records of ocean-bottom seismometers: Results from year one of the Cascadia Initiative. *Bull. Seismol. Soc. Am.* **105**, 300-313 (2014).
42. Helffrich, G. Extended-time multitaper frequency domain cross-correlation receiver-function estimation. *Bull. Seismol. Soc. Am.* **96**, 344-347 (2006).
43. Rychert, C. A., Laske, G., Harmon, N., & Shearer, P. M. Seismic imaging of melt in a displaced Hawaiian plume. *Nat. Geosci.* **6**, 657 (2013).
44. Efron, B., & Tibshirani, R. Statistical data analysis in the computer age. *Science* **253**, 390-395 (1991).
45. Schmandt, B., Jacobsen, S. D., Becker, T. W., Liu, Z., & Dueker, K. G. Dehydration melting at the top of the lower mantle. *Science* **344**, 1265-1268 (2014).
46. Bina, C. R., & Helffrich, G. Phase transition Clapeyron slopes and transition zone seismic discontinuity topography. *J. Geophys. Res.* **99**, 15853-15860 (1994).
47. Ye, Y., Gu, C., Shim, S. H., Meng, Y., & Prakapenka, V. The postspinel boundary in pyrolitic compositions determined in the laser-heated diamond anvil cell. *Geophys. Res. Lett.* **41**, 3833-3841 (2014).
48. Litasov, K. D., Ohtani, E., & Sano, A. Influence of water on major phase transitions in the Earth's mantle. *Geophys. Monogr.-Am. Geophys. Un.* **168**, 95 (2006).
49. Lebedev, S., Chevrot, S., & van der Hilst, R. D. Seismic evidence for olivine phase changes at the 410-and 660-kilometer discontinuities. *Science* **296**, 1300-1302 (2002).

50. Akaogi, M., Ito, E., & Navrotsky, A. Olivine-modified spinel-spinel transitions in the system Mg2SiO4-Fe2SiO4: Calorimetric measurements, thermochemical calculation, and geophysical application. *J. Geophys. Res.* **94**, 15671-15685 (1989).
51. Ito, E., Akaogi, M., Topor, L., & Navrotsky, A. Negative pressure-temperature slopes for reactions forming MgSiO3 perovskite from calorimetry. *Science* **249**, 1275-1278 (1990).
52. Houser, C. Global seismic data reveal little water in the mantle transition zone. *Earth Planet. Sci. Lett.* **448**, 94-101 (2016).
53. Anderson, D. L., Schramm, K. A., Foulger, G. R., Natland, J. H., & Presnall, D. C. Global hotspot maps. *Geol. Soc. Spec. Pap.* **388**, 19 (2005).
54. Durand, S., Debayle, E., Ricard, Y., Zaroli, C., & Lambotte, S.. Confirmation of a change in the global shear velocity pattern at around 1000 km depth. *Geophys. J. Int.* **211**(3), 1628-1639 (2017).
55. French, S. W., & Romanowicz, B. A. Whole-mantle radially anisotropic shear velocity structure from spectral-element waveform tomography. *Geophys. J. Int.* **199**(3), 1303-1327 (2014).
56. Tesoniero, A., Auer, L., Boschi, L., & Cammarano, F. Hydration of marginal basins and compositional variations within the continental lithospheric mantle inferred from a new global model of shear and compressional velocity. *J. Geophys. Res.* **120**(11), 7789-7813 (2015).
57. Moulik, P., & Ekström, G. An anisotropic shear velocity model of the Earth's mantle using normal modes, body waves, surface waves and long-period waveforms. *Geophys. J. Int.* **199**(3), 1713-1738 (2014).
58. Colli, L., Fichtner, A., & Bunge, H. P. Full waveform tomography of the upper mantle in the South Atlantic region: Imaging a westward fluxing shallow asthenosphere? *Tectonophysics*, ***604***, 26-40 (2013).
59. Shen, Y., Solomon, S. C., Bjarnason, I. T., & Wolfe, C. J. Seismic evidence for a lower-mantle origin of the Iceland plume. *Nature* **395**, 62 (1998).

Extended Data

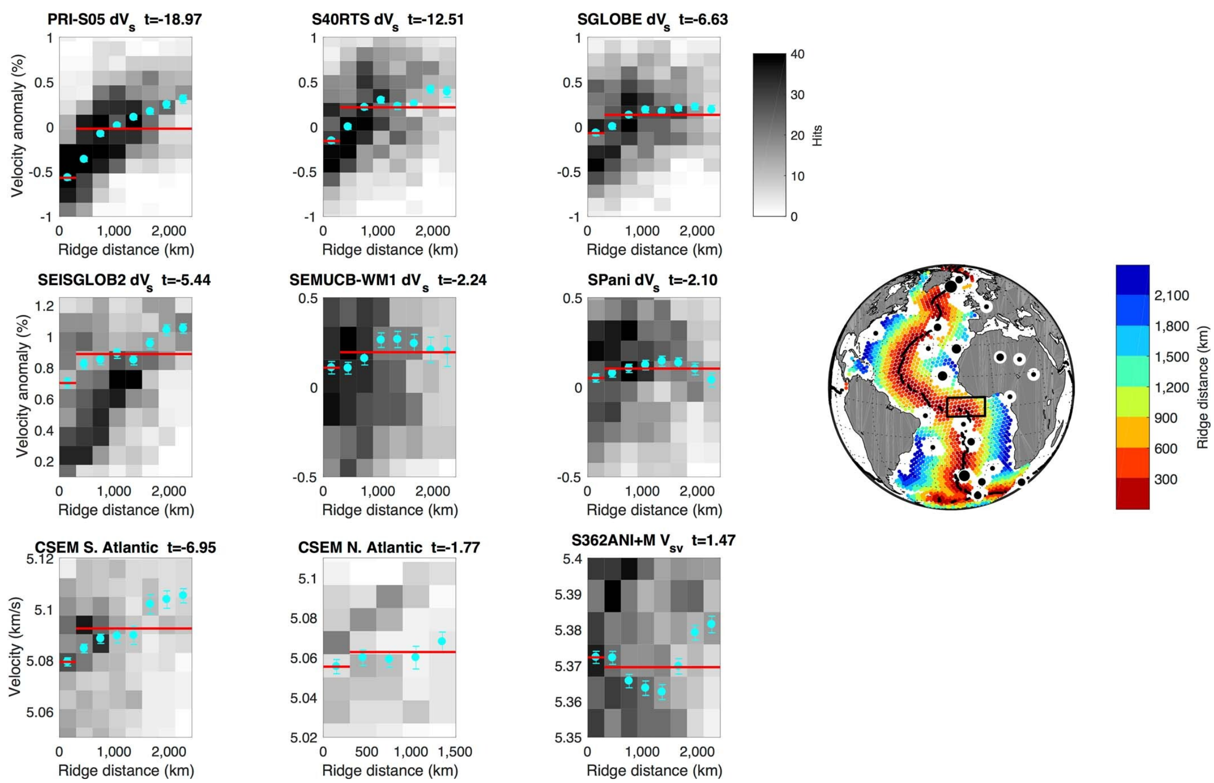

Extended Data Figure 1 | Relationship of MTZ shear velocity with distance to ridge. Distance binned average velocity of the mantle transition zone for global and regional models[4,5,7,9,54,55,56,57,58]. Bin averages are shown as cyan circles, with error bars showing the standard error of the mean. Red lines show the averages for distances < 300 km and > 300 km. Background shading shows a 2-D histogram of transition zone velocities. Model name and t-statistic are given in the title of each panel. Probability at 95% occurs when the absolute value of the t-statistic is > 1.67, 99% occurs at a value > 2.37 for the given degrees of freedom. Negative t-statistics indicate that the mean of the sub-ridge bin is less than that of the mean of more distant bins. Map shows the distance to ridge binning as coloured circles, with the MAR shown in black. White circles centred on black dots show the hotspot locations, with the size of the black circle proportional to the rating[29,53]. Black box shows our study area.

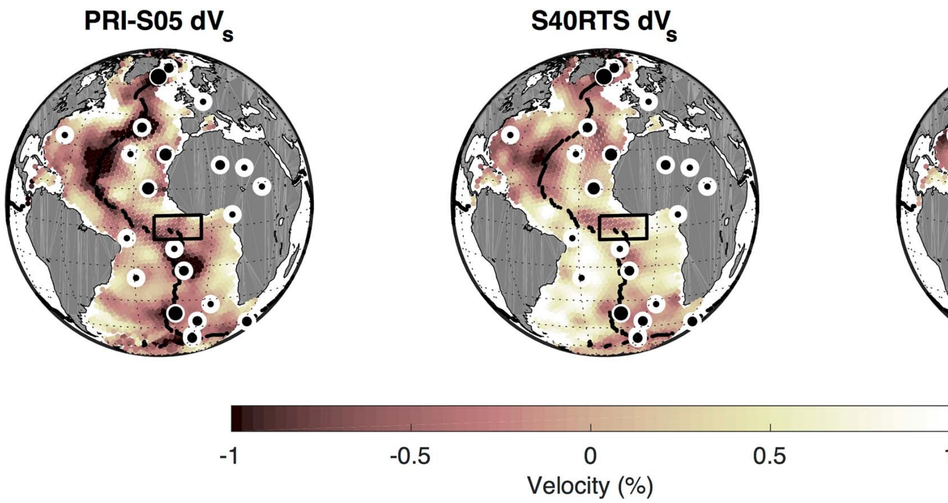

Extended Data Figure 2 | Global shear-velocity models of the mantle transition zone. The three models PRI-S05[7], S40RTS[5] and SGLOBE[4] show average MTZ shear-velocities beneath the Atlantic ocean. The Mid-Atlantic Ridge is shown in black. White circles centred on black dots show the hotspot locations, with the size of the black circle proportional to their rating[29,53]. Black box shows our study area.

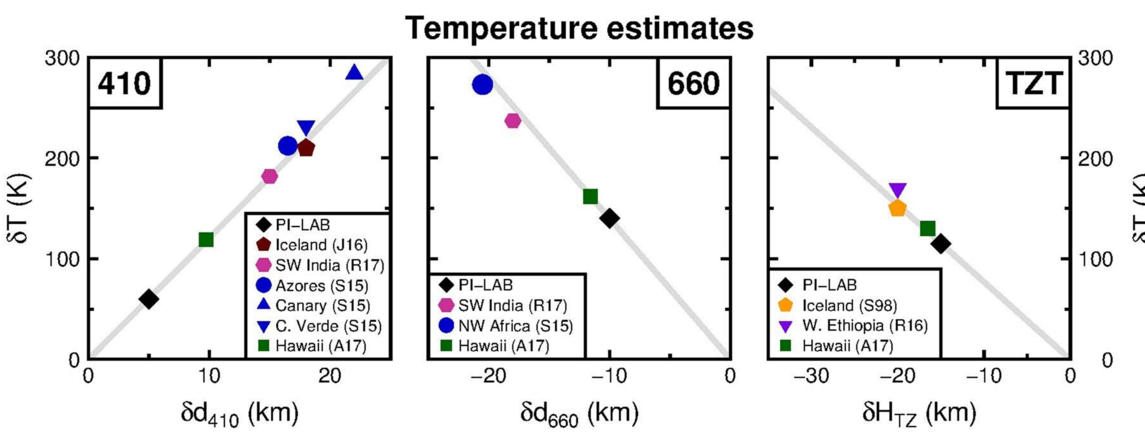

Extended Data Figure 3 | Temperature estimates from relationships with respect to the 410- and 660-km depth discontinuity topography, and mantle transition zone thickness (TZT). Grey lines are the Clapeyron slopes +2.9 MPa/K[46], -2.5 MPa/K[47] and -0.13 km/K[49] for the 410, 660 and TZT, respectively. Black diamonds: Estimates from this study. Other symbols: Average estimates from Azores, Canary, Cape Verde and north-west Africa[28], Iceland (orange[59] and brown[31] pentagon), Southwest Indian Ridge[27] and Hawaii[32].

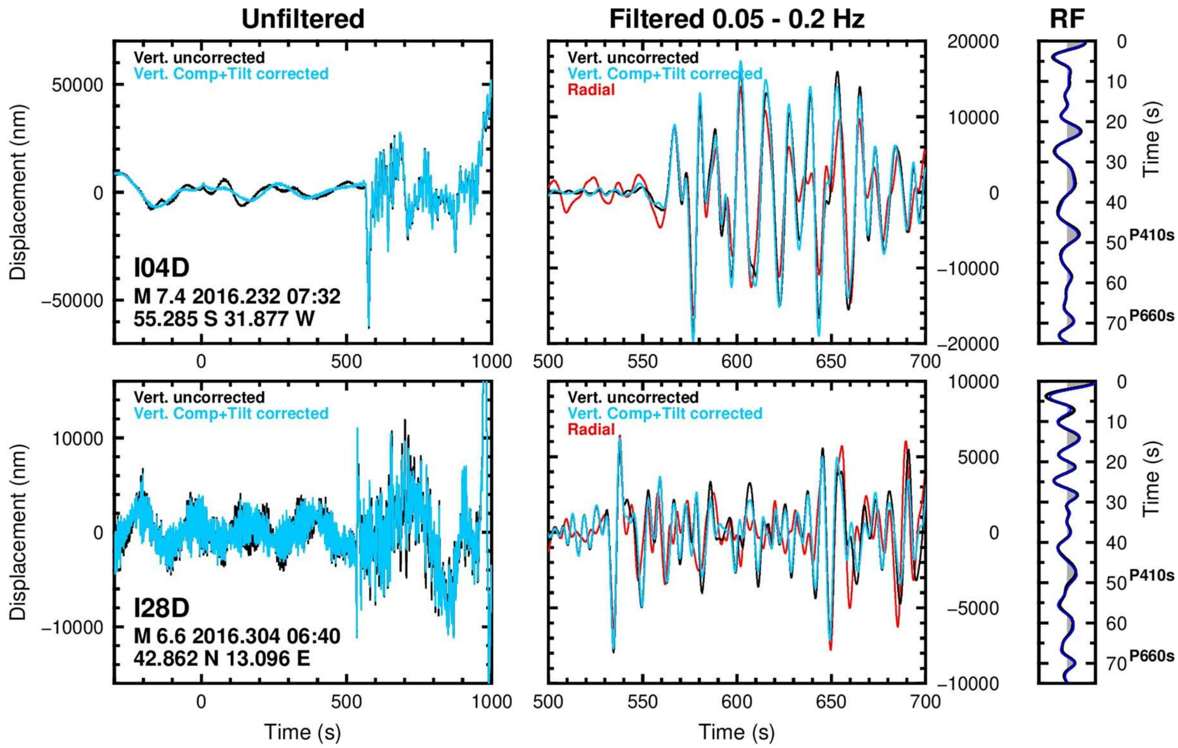

Extended Data Figure 4 | Example of waveform corrections and receiver functions. Left panels show the unfiltered and uncorrected (black) and the tilt and compliance corrected (cyan) vertical waveforms of a recorded earthquake. Middle: Zoomed in, filtered waveforms also showing the radial (red) component. Right: Receiver functions from the deconvolution of the vertical uncorrected (black) and corrected (blue) component with the radial component, here essentially identical for corrected and uncorrected data. Top and bottom: Example of waveforms from a magnitude 7.4 and 6.6 earthquake, respectively.

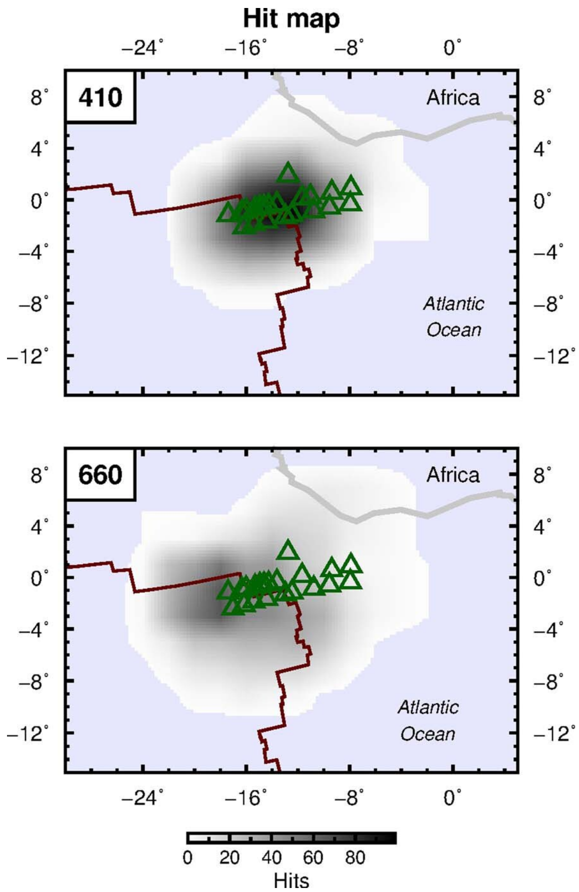

598

599 **Extended Data Figure 5 | Hit maps showing the number of measurements at 410 and 660-**
600 **km depths.** Grey shade indicates the coverage. Red line: Mid-Atlantic Ridge[37].

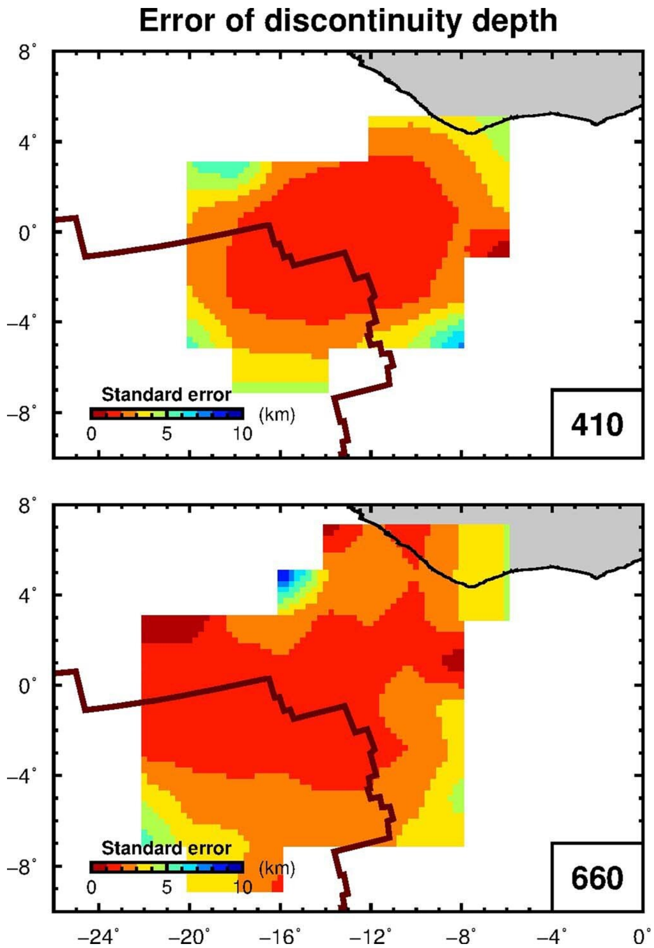

Extended Data Figure 6 | Depth errors of the 410- and 660-km discontinuities. Standard errors are determined from the depth migration of each waveform. Red line: Mid-Atlantic Ridge[37].

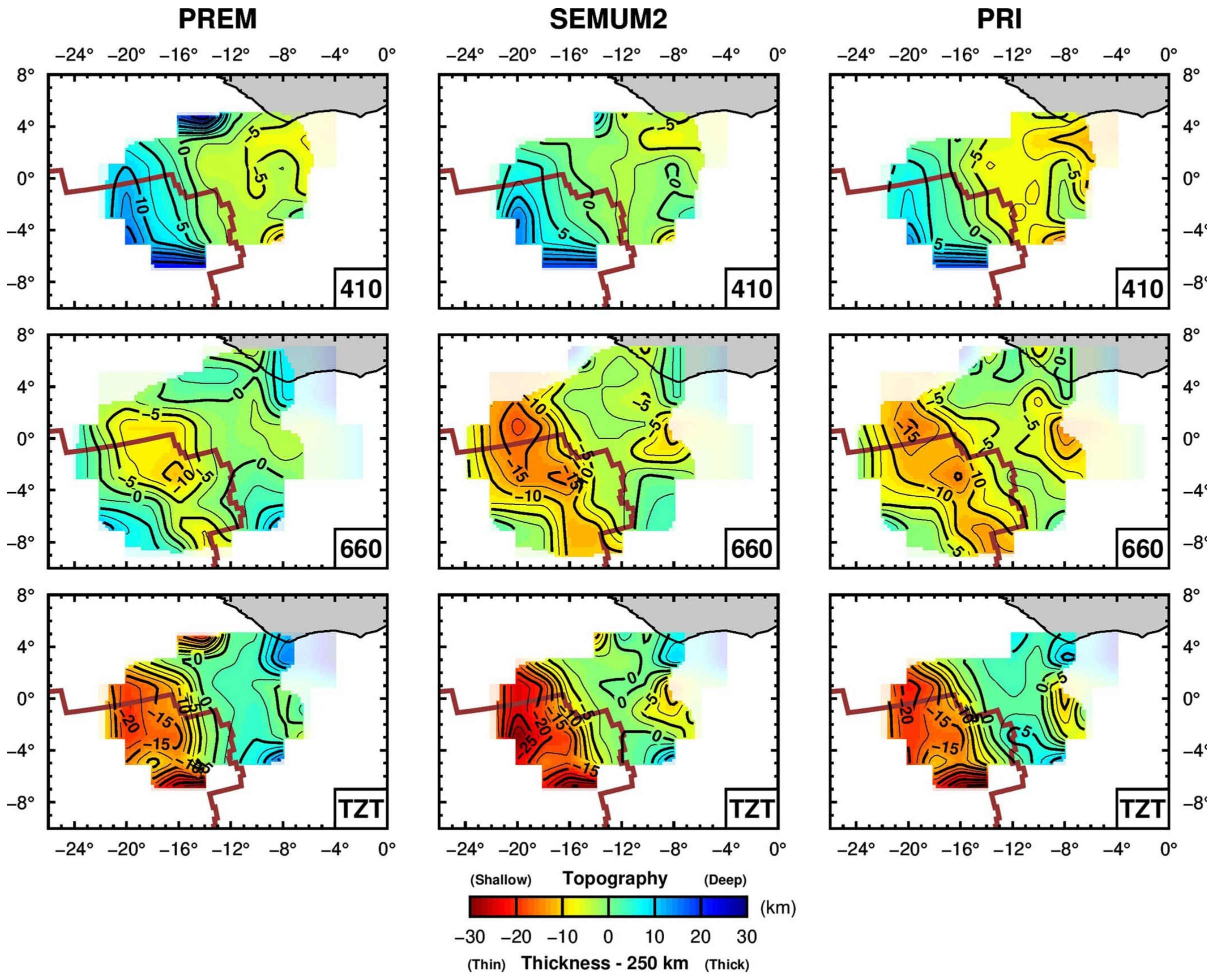

Extended Data Figure 7 | Migration tests. Receiver function migration tests using 1D crust-corrected PREM[8] and 3D models SEMUM2[6] (using PREM V_P/V_S ratio for V_P) and PRI-P05 and PRI-S05[7]. Horizontal cross-sections from the 3-D depth migration: 410-, 660-km depth discontinuities and mantle Transition Zone Thickness (TZT) (top, middle and bottom, respectively). Semi-transparent shades are poorly constrained areas. Red line: Mid-Atlantic Ridge[37].

All References (main text and online Methods)

1 Van der Hilst, R. D. Complex morphology of subducted lithosphere in the mantle beneath the Tonga trench. *Nature* **374**, 154-157 (1995).

2 Montelli, R., Nolet, G., Dahlen, F. A., Masters, G., Engdahl, E. R., & Hung, S. H. Finite-frequency tomography reveals a variety of plumes in the mantle. *Science* **303**, 338-343 (2004).

3 Hofmann, A. W. Mantle geochemistry: the message from oceanic volcanism. *Nature* **385**, 219 (1997).

4 Chang, S. J., Ferreira, A. M., Ritsema, J., van Heijst, H. J., & Woodhouse, J. H. Joint inversion for global isotropic and radially anisotropic mantle structure including crustal thickness perturbations. *J. Geophys. Res*. **120**(6), 4278-4300 (2015).

5 Ritsema, J., Deuss, A. A., Van Heijst, H. J., & Woodhouse, J. H. S40RTS: a degree-40 shear-velocity model for the mantle from new Rayleigh wave dispersion, teleseismic traveltime and normal-mode splitting function measurements. *Geophys. J. Int.* **184**, 1223-1236 (2011).

6 French, S., Lekic, V., & Romanowicz, B. Waveform tomography reveals channeled flow at the base of the oceanic asthenosphere. *Science* **342**, 227-230 (2013).

7 Montelli, R., Nolet, G., Dahlen, F. A., & Masters, G. A catalogue of deep mantle plumes: New results from finite-frequency tomography. *Geochem. Geophys. Geosyst.* **7**(11) (2006).

8 Dziewonski, A. M., & Anderson, D. L. Preliminary reference Earth model. *Phys. Earth Planet Inter.* **25**, 297-356 (1981).

9 Rickers, F., Fichtner, A., & Trampert, J. The Iceland–Jan Mayen plume system and its impact on mantle dynamics in the North Atlantic region: evidence from full-waveform inversion. *Earth Planet. Sci. Lett.* **367**, 39-51 (2013).

10 French, S. W., & Romanowicz, B. Broad plumes rooted at the base of the Earth's mantle beneath major hotspots. *Nature* **525**, 95-99 (2015).

11 Fukao, Y., & Obayashi, M. Subducted slabs stagnant above, penetrating through, and trapped below the 660 km discontinuity. *J. Geophys. Res.* **118**, 5920-5938 (2013).

12 Li, C., van der Hilst, R. D., Engdahl, E. R., & Burdick, S. A new global model for P wave speed variations in Earth's mantle. *Geochem. Geophys. Geosyst.* **9**(5) (2008).

13 Ito, E., & Katsura, T. A temperature profile of the mantle transition zone. *Geophys. Res. Lett.* **16**, 425-428 (1989).

14 Lawrence, J. F., & Shearer, P. M. Imaging mantle transition zone thickness with SdS-SS finite-frequency sensitivity kernels. *Geophys. J. Int.* **174**, 143-158 (2008).

15 Houser, C., Masters, G., Flanagan, M., & Shearer, P. Determination and analysis of long-wavelength transition zone structure using SS precursors. *Geophys. J. Int.* **174**, 178-194 (2008).

16 Morgan, J. P., & Morgan, W. J. Two-stage melting and the geochemical evolution of the mantle: a recipe for mantle plum-pudding. *Earth Planet. Sci. Lett.*, **170**(3), 215-239 (1999).

17 Jellinek, A. M., & Manga, M. The influence of a chemical boundary layer on the fixity, spacing and lifetime of mantle plumes. *Nature* **418**, 760-763 (2002).

18 Jellinek, A. M., & Manga, M. Links between long-lived hot spots, mantle plumes, d″, and plate tectonics. *Rev. Geophys.* **42**(3) (2004).

19 McNamara, A. K., & Zhong, S. Thermochemical structures beneath Africa and the Pacific Ocean. *Nature* **437**, 1136-1139 (2005).

20 Kellogg, L. H., Hager, B. H., & van der Hilst, R. D. Compositional stratification in the deep mantle. *Science* **283**, 1881-1884 (1999).

21 Ballmer, M. D., Schmerr, N. C., Nakagawa, T., & Ritsema, J. Compositional mantle layering revealed by slab stagnation at~ 1000-km depth. *Sci. Adv.* **1**(11) (2015).

22 Marquardt, H., & Miyagi, L. Slab stagnation in the shallow lower mantle linked to an increase in mantle viscosity. *Nat. Geosci.* **8**, 311-314 (2015).

23 Ballmer, M. D., Houser, C., Hernlund, J. W., Wentzcovitch, R. M., & Hirose, K. Persistence of strong silica-enriched domains in the Earth's lower mantle. *Nat. Geosci.* **10**, 236-240 (2017).

24 Bercovici, D., & Karato, S. I. Whole-mantle convection and the transition-zone water filter. *Nature* **425** (2003).

25 Lawrence, J. F., & Shearer, P. M. A global study of transition zone thickness using receiver functions. *J. Geophys. Res.* **111** (2006).

26 Shen, Y., Sheehan, A. F., Dueker, K. G., de Groot–Hedlin, C., & Gilbert, H. Mantle discontinuity structure beneath the southern East Pacific Rise from P-to-S converted phases. *Science* **280**, 1232-1235 (1998).

27 Ruan, A., Hu, H., Li, J., Niu, X., Wei, X., Zhang, J., & Wang, A. Crustal structure and mantle transition zone thickness beneath a hydrothermal vent at the ultra-slow spreading Southwest Indian Ridge (49° 39′ E): a supplementary study based on passive seismic receiver functions. *Mar. Geophys. Res.* **38**, 39-46 (2017).

28 Saki, M., Thomas, C., Nippress, S. E., & Lessing, S. Topography of upper mantle seismic discontinuities beneath the North Atlantic: The Azores, Canary and Cape Verde plumes. *Earth Planet. Sci. Lett.* **409**, 193-202 (2015).

29 Courtillot, V., Davaille, A., Besse, J., & Stock, J. Three distinct types of hotspots in the Earth's mantle. *Earth Planet. Sci. Lett.* **205**, 295-308 (2003).

30 Le Voyer, M., Cottrell, E., Kelley, K. A., Brounce, M., & Hauri, E. H. The effect of primary versus secondary processes on the volatile content of MORB glasses: An example from the equatorial Mid-Atlantic Ridge (5°N–3°S). *J. Geophys. Res.* **120**, 125-144 (2015).

31 Jenkins, J., Cottaar, S., White, R. S., & Deuss, A. Depressed mantle discontinuities beneath Iceland: Evidence of a garnet controlled 660 km discontinuity? *Earth Planet. Sci. Lett.* **433**, 159-168 (2016).

32 Agius, M. R., Rychert, C. A., Harmon, N., & Laske, G. Mapping the mantle transition zone beneath Hawaii from Ps receiver functions: Evidence for a hot plume and cold mantle downwellings. *Earth Planet. Sci. Lett.* **474**, 226-236 (2017).

33 Thomson, A. R., Walter, M. J., Kohn, S. C., & Brooker, R. A. Slab melting as a barrier to deep carbon subduction. *Nature* **529**, 76 (2016).

34 Dalton, C. A., Langmuir, C. H., & Gale, A. Geophysical and geochemical evidence for deep temperature variations beneath mid-ocean ridges. *Science* **344**, 80-83 (2014).

35 Richter, F. M. Convection and the large-scale circulation of the mantle. *J. Geophys. Res.*, **78**, 8735-8745 (1973).

36 Schilling, J. G., Hanan, B. B., McCully, B., Kingsley, R. H., & Fontignie, D. Influence of the Sierra Leone mantle plume on the equatorial Mid-Atlantic Ridge: A Nd-Sr-Pb isotopic study. *J. Geophys. Res.* **99**, 12005-12028 (1994).

37 Bird, P. An updated digital model of plate boundaries. *Geochem. Geophys. Geosyst.* **4** (2003).

38 Agius, M. R., Harmon, N., Rychert, C. A., Tharimena, S., & Kendall, J. M. Sediment characterization at the equatorial Mid-Atlantic Ridge from P-to-S teleseismic phase conversions recorded on the PI-LAB experiment. *Geophys. Res. Lett.* **45**, 12-244 (2018).

39 Harmon, N., Rychert, C., Agius, M., Tharimena, S., Le Bas, T., Kendall, J. M., & Constable, S. Marine geophysical investigation of the chain fracture zone in the Equatorial Atlantic from the PI-LAB experiment. *J. Geophys. Res.* **123**, 11-016 (2018).

40 Crawford, W. C., & Webb, S. C. Identifying and removing tilt noise from low-frequency (< 0.1 Hz) seafloor vertical seismic data. *Bull. Seismol. Soc. Am.* **90**, 952-963 (2000).

41 Bell, S. W., Forsyth, D. W., & Ruan, Y. Removing noise from the vertical component records of ocean-bottom seismometers: Results from year one of the Cascadia Initiative. *Bull. Seismol. Soc. Am.* **105**, 300-313 (2014).

42 Helffrich, G. Extended-time multitaper frequency domain cross-correlation receiver-function estimation. *Bull. Seismol. Soc. Am.* **96**, 344-347 (2006).

43 Rychert, C. A., Laske, G., Harmon, N., & Shearer, P. M. Seismic imaging of melt in a displaced Hawaiian plume. *Nat. Geosci.* **6**, 657 (2013).

44 Efron, B., & Tibshirani, R. Statistical data analysis in the computer age. *Science* **253**, 390-395 (1991).

45 Schmandt, B., Jacobsen, S. D., Becker, T. W., Liu, Z., & Dueker, K. G. Dehydration melting at the top of the lower mantle. *Science* **344**, 1265-1268 (2014).

46 Bina, C. R., & Helffrich, G. Phase transition Clapeyron slopes and transition zone seismic discontinuity topography. *J. Geophys. Res.* **99**, 15853-15860 (1994).

47 Ye, Y., Gu, C., Shim, S. H., Meng, Y., & Prakapenka, V. The postspinel boundary in pyrolitic compositions determined in the laser-heated diamond anvil cell. *Geophys. Res. Lett.* **41**, 3833-3841 (2014).

48 Litasov, K. D., Ohtani, E., & Sano, A. Influence of water on major phase transitions in the Earth's mantle. *Geophys. Monogr.-Am. Geophys. Un.* **168**, 95 (2006).

49 Lebedev, S., Chevrot, S., & van der Hilst, R. D. Seismic evidence for olivine phase changes at the 410-and 660-kilometer discontinuities. *Science* **296**, 1300-1302 (2002).

50 Akaogi, M., Ito, E., & Navrotsky, A. Olivine-modified spinel-spinel transitions in the system Mg2SiO4-Fe2SiO4: Calorimetric measurements, thermochemical calculation, and geophysical application. *J. Geophys. Res.* **94**, 15671-15685 (1989).

51 Ito, E., Akaogi, M., Topor, L., & Navrotsky, A. Negative pressure-temperature slopes for reactions forming MgSiO3 perovskite from calorimetry. *Science* **249**, 1275-1278 (1990).

52 Houser, C. Global seismic data reveal little water in the mantle transition zone. *Earth Planet. Sci. Lett.* **448**, 94-101 (2016).

53 Anderson, D. L., Schramm, K. A., Foulger, G. R., Natland, J. H., & Presnall, D. C. Global hotspot maps. *Geol. Soc. Spec. Pap.* **388**, 19 (2005).

54 Durand, S., Debayle, E., Ricard, Y., Zaroli, C., & Lambotte, S.. Confirmation of a change in the global shear velocity pattern at around 1000 km depth. *Geophys. J. Int.* **211**(3), 1628-1639 (2017).

55 French, S. W., & Romanowicz, B. A. Whole-mantle radially anisotropic shear velocity structure from spectral-element waveform tomography. *Geophys. J. Int.* **199**(3), 1303-1327 (2014).

56 Tesoniero, A., Auer, L., Boschi, L., & Cammarano, F. Hydration of marginal basins and compositional variations within the continental lithospheric mantle inferred from a new global model of shear and compressional velocity. *J. Geophys. Res.* **120**(11), 7789-7813 (2015).

57 Moulik, P., & Ekström, G. An anisotropic shear velocity model of the Earth's mantle using normal modes, body waves, surface waves and long-period waveforms. *Geophys. J. Int.* **199**(3), 1713-1738 (2014).

58 Colli, L., Fichtner, A., & Bunge, H. P. Full waveform tomography of the upper mantle in the South Atlantic region: Imaging a westward fluxing shallow asthenosphere? *Tectonophysics*, ***604***, 26-40 (2013).

59 Shen, Y., Solomon, S. C., Bjarnason, I. T., & Wolfe, C. J. Seismic evidence for a lower-mantle origin of the Iceland plume. *Nature* **395**, 62 (1998).